Supporting Information

Coke-resistant Ni-based bimetallic catalysts for dry reforming methane: effects of indium on the Ni/Al_2O_3 catalyst

Chuanshen Wang, Tongming Su, Zuzeng Qin*, and Hongbing Ji*

School of Chemistry and Chemical Engineering, Guangxi Key Laboratory of Petrochemical Resource Processing and Process Intensification Technology, Guangxi University, Nanning, 530004, China

* Corresponding author. E-mail: qinzuzeng@gxu.edu.cn (Z. Q.); jihb@mail.sysu.edu.cn (H. J.)

Experimental

Catalysts characterization

H_2 temperature-programmed reduction (H_2-TPR) were performed on an AMI-300 catalyst characterization system equipped with the TCD detector was set to 100 °C and the bridge current was set to 75 mA. 50 mg samples were pre-treated in an Ar flow (30 ml min^{-1}) for 1 h at 300 °C to remove water and impurities in the catalyst, then switch to 10 vol% H_2/Ar (30 ml min^{-1}) by valve actuation and wait for the baseline to stabilize. The temperature is increased from 50 °C to 1000 °C with a temperature ramping rate of 10 °C min^{-1},the tail gas is fed into the TCD detector to record the data.

CO_2 temperature programmed desorption (CO_2-TPD) conducted using AMI-300 catalyst characterization system equipped with the TCD detector was set to 100 °C and the bridge current was set to 135 mA. 100 mg sample were pre-treated in an Ar flow (30 ml min^{-1}) at 300 °C for 1 h, then warmed to 800 °C for reduction for 1 h. After the reduction, the system was cooled to 50 °C and switched to CO_2 (30 ml min^{-1}) for static adsorption for 1 hour until saturation. Afterwards, the sample was purged with He (30 ml min^{-1}) until baseline stable, later the temperature was risen from 50 °C to 800 °C with a temperature ramping rate of 10 °C min^{-1},the tail gas is fed into the TCD detector to record the data.

NH_3 temperature programmed desorption (NH_3-TPD) also conducted using AMI-300 catalyst characterization system equipped with the TCD detector was set to 100 °C and the bridge current was set to 135 mA. Samples (100 mg) were pre-treated were pre-treated in an Ar flow (30 ml min^{-1}) at 300 °C for 1 h, then warmed to 800 °C for reduction for 1 h. After the reduction, the system was cooled to 100 °C and switched to NH_3 (30 ml min^{-1}) for static

adsorption for 1 hour until saturation. Afterwards, the sample was purged with He (30 ml min^{-1}) until baseline stable, later the temperature was risen from 100 °C to 800 °C with a temperature ramping rate of 10 °C min^{-1},the tail gas is fed into the TCD detector to record the data.

H_2 chemisorption were performed on an AMI-300 catalyst characterization system equipped with the TCD detector was set to 100 °C and the bridge current was set to 75 mA. 200 mg sample were pre-treated in an Ar flow (30 ml min^{-1}) at 300 °C for 1 h, then warmed to 800 °C for reduction for 1 h. After the reduction, the system was cooled to 50 °C and was purged with Ar (30 ml min^{-1}) until baseline stable. Afterwards, switched to 10 % H_2/Ar is pulsed in 20 times and the tail gas enters the TCD detector to collect data. The difference between the measured stable H_2 absorption peak area and the absorption peak area of each pulse is the total amount of H_2 chemisorbed and the degree of dispersion of the active metal on the catalyst surface can be obtained by calculation. The calculation formula is shown in Eq (4).

Table S1 The fitting results of surface oxygen species on the basis of O 1s spectra over the reduced catalysts.

Sample	O_α		O_β		O_γ	
	BE (eV)	Area (%)	BE (eV)	Area (%)	BE (eV)	Area (%)
Ni/Al_2O_3	531.78	73.5	533.24	19.9	534.27	6.60
In/Al_2O_3	531.15	55.6	532.17	34.4	533.38	10.0
$3Ni\text{-}2In/Al_2O_3$	530.73	64.9	531.92	29.9	533.25	5.20

Table S2 NH_3 desorption amount of the support and catalysts

Sample	NH_3 desorption ($\mu mol/g_{cat}$)
Al_2O_3	315
Ni/Al_2O_3	468
In/Al_2O_3	302
$4Ni\text{-}1In/Al_2O_3$	437
$3Ni\text{-}2In/Al_2O_3$	407
$2Ni\text{-}3In/Al_2O_3$	406
$1Ni\text{-}4In/Al_2O_3$	390

Table S3 Activity comparison of the Ni-based catalysts for DRM.

Catalyst	WHSV ($mL\ h^{-1}\ g_{cat}^{-1}$)	CH_4/CO_2/inert gas	CH_4 conversion (%)	Temperature (°C)	Reference
Ni/Al_2O_3	18000	$1CH_4/1CO_2/1N_2$	78.8	700	This work
In/Al_2O_3	18000	$1CH_4/1CO_2/1N_2$	9.1	700	
$1Ni\text{-}4In/Al_2O_3$	18000	$1CH_4/1CO_2/1N_2$	6.5	700	
$2Ni\text{-}3In/Al_2O_3$	18000	$1CH_4/1CO_2/1N_2$	21.6	700	
$3Ni\text{-}2In/Al_2O_3$	18000	$1CH_4/1CO_2/1N_2$	91.1	700	
$4Ni\text{-}1In/Al_2O_3$	18000	$1CH_4/1CO_2/1N_2$	66.8	700	
$In_{0.5}Ni@SiO_2$	18000	$1CH_4/1CO_2$	92	800	1
$Ni\text{-}In/Al_2O_3$	21000	$49.5CH_4/49.5CO_2/1Ar$	28	650	2
$Ni\text{-}In/Ce\text{-}Al_2O_3$	21000	$49.5CH_4/49.5CO_2/1Ar$	25	650	
$Ni\text{-}In/SiO_2$	40000	$69CH_4/30CO_2/1Ar$	19.5	600	3
2.5Co-2.5Ni@SGA	36000	$1CH_4/1CO_2/1Ar$	30	600	4
$(NiMg)_4Al$	3840000	$1CH_4/1CO_2/2N_2$	69.8	900	5
$Ni5/MgAl_2O_4(SA)$	60000	$1CH_4/1CO_2/3N_2$	93.0	750	6
	60000	$1CH_4/1CO_2/3N_2$	74.2	650	
$12\%Ni/Mg_3Al$	60000	$1CH_4/1CO_2/2N_2$	88	750	7
$Ni\text{-}Ce/ZrO_2$	24000	$1CH_4/1CO_2$	55	700	8
$Ni\text{-}Y/ZrO_2$	24000	$1CH_4/1CO_2$	70	700	
$Ni\text{-}P/Al_2O_3$	18000	$1CH_4/1CO_2/1Ar$	84	750	9
$Ni\text{-}2P/Al_2O_3$	18000	$1CH_4/1CO_2/1Ar$	65	750	
$Hollow\text{-}NiPt/SiO_2$	60000	$1CH_4/1CO_2/1N_2$	94.9	800	10
$Mo/Ni/Al_2O_3\text{-}CeO_2$	12000	$1CH_4/1CO_2$	72	700	11
$0.01\ \%Rh/Al_2O_3$	12000	$47CH_4/47CO_2/6N_2$	83	750	12
$Ni/ZrO_2\text{-}Al_2O_3$	25000	$1CH_4/1CO_2$	58	700	13
$Co\text{-}Al/ZrO_2$	60000	$2CH_4/2CO_2/1N_2$	67.6	850	14
$Ni\text{-}Co/SiO_2$	50000	$1CH_4/1CO_2/8He$	80	700	15
Ga/MCM-41	39000	$30CH_4/30CO_2/5N_2$	85	800	16
$NiMg_1Al_1$	80000	$1CH_4/1CO_2$	83	800	17
$NaOH\ Ni/MgO\text{-}Al_2O_3$	48000	$1CH_4/1CO_2/2N_2$	91	800	18

Table S4 I_D/I_G ratios obtained from carbon-related peaks for each of the samples subjected to DRM reaction.

Sample	I_D/I_G
Ni/Al_2O_3	1.19
In/Al_2O_3	1.35
$3Ni\text{-}2In/Al_2O_3$	0.44

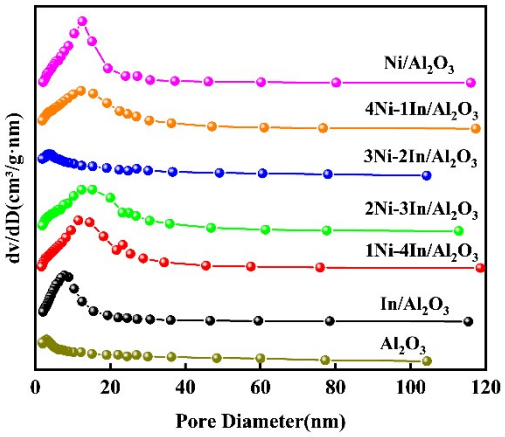

Fig. S1 The pore size distribution curves of the support and catalysts.

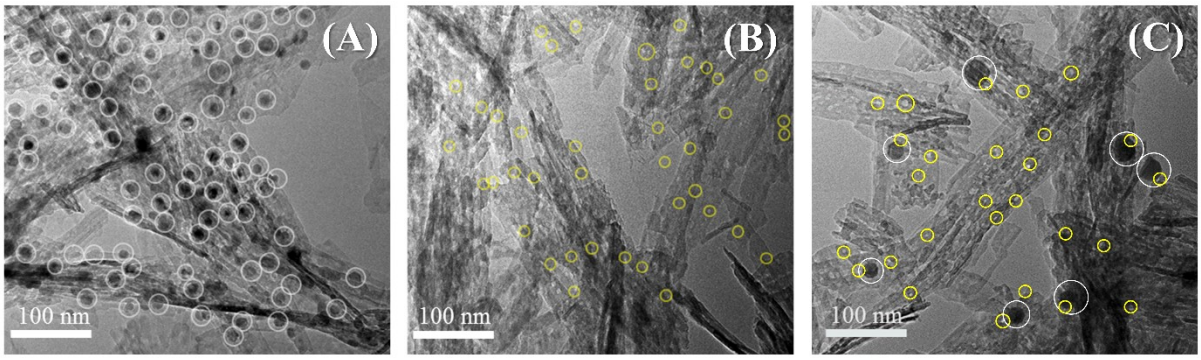

Fig. S2 TEM images of reduced Ni/Al_2O_3 (A), In/Al_2O_3 (B), and $3Ni\text{-}2In/Al_2O_3$ (C) (Ni and In particles are marked with white and yellow lines, respectively).

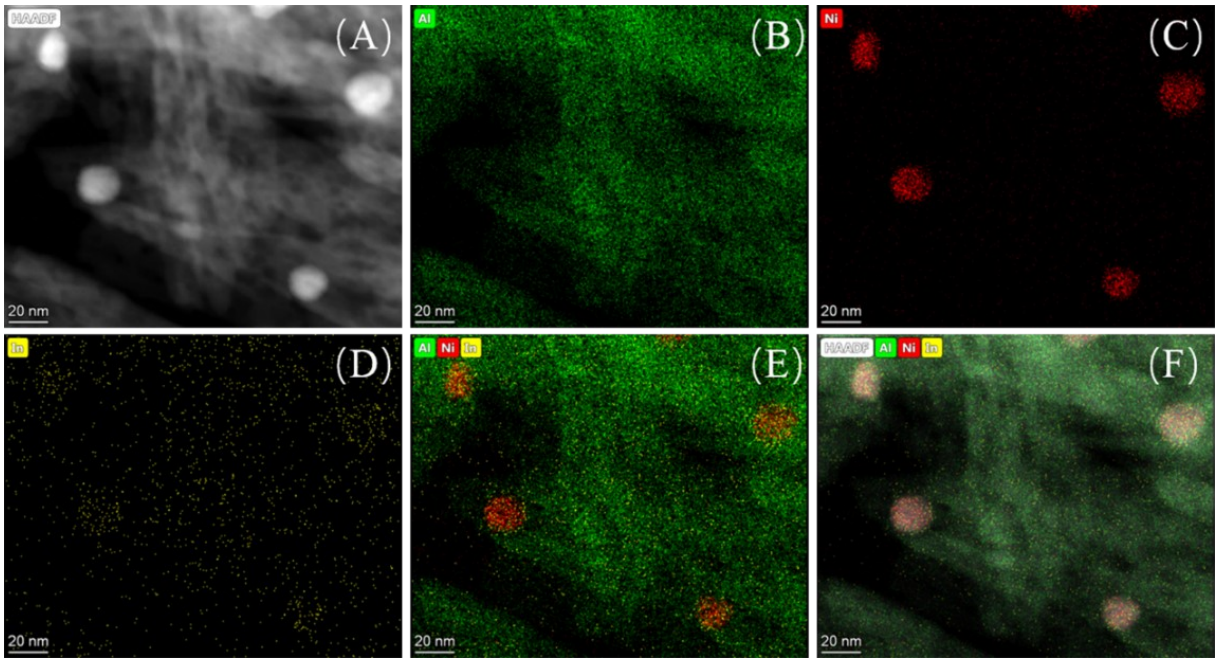

Fig. S3 HAADF-STEM image (A) and EDS profile of Al (B), Ni (C), In (D), and merged images (E) and (F) in reduced Ni-In/Al_2O_3 catalyst.

The composition of the reduced bimetallic particles in the catalyst was determined using scanning TEM (STEM) coupled with energy-dispersive X-ray spectroscopy (EDS), as shown in Fig. S3. The high-angle annular dark-field (HAADF) STEM image in Fig. S3A and EDS elemental mappings of Ni in Fig. S3C shows a clear agglomeration of Ni nanoparticles on the support surface due to the high temperature reduction process. According to EDS elemental mappings in Fig. S3B, the spatial distribution of Al is uniform. The agglomeration of Ni also affects the distribution of In particles, In particles also display a trend of partial concentration of distribution due to the interaction between Ni and In (Fig. S3D), and the merged image (Fig. S3E) further confirms the distribution of In was influenced by Ni.

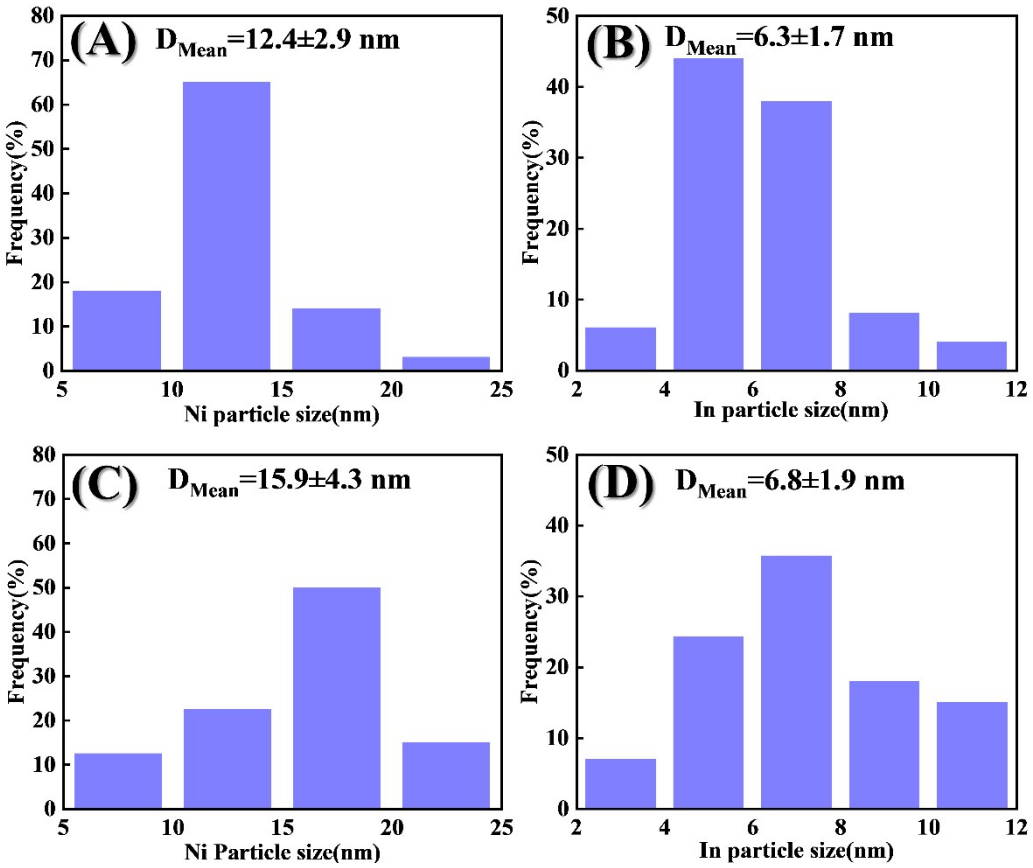

Fig. S4 Particle size distributions of Ni and In in the (A) Ni/Al_2O_3, (B) In/Al_2O_3, (C) and (D) $3Ni\text{-}2In/Al_2O_3$ catalyst.

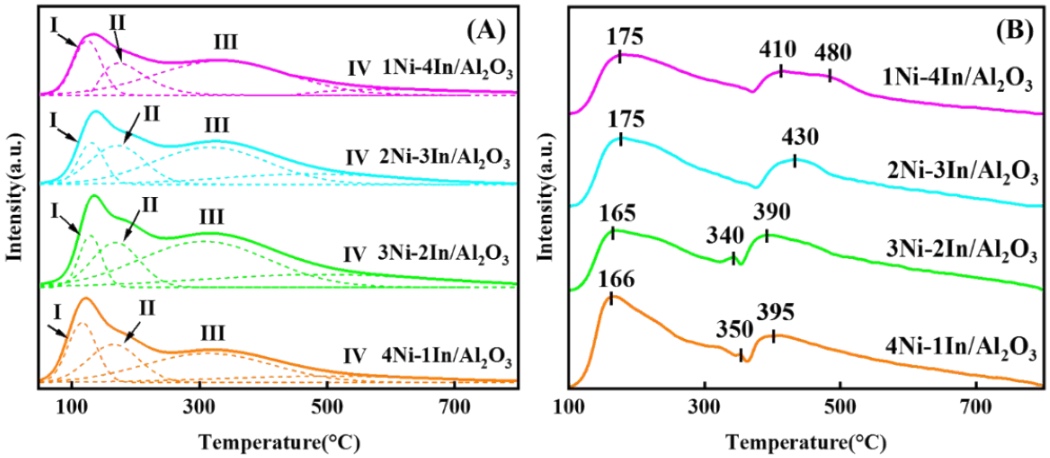

Fig. S5 (A) CO_2-TPD and (B) NH_3-TPD curves of fresh calcined catalysts with different Ni-In ratios.

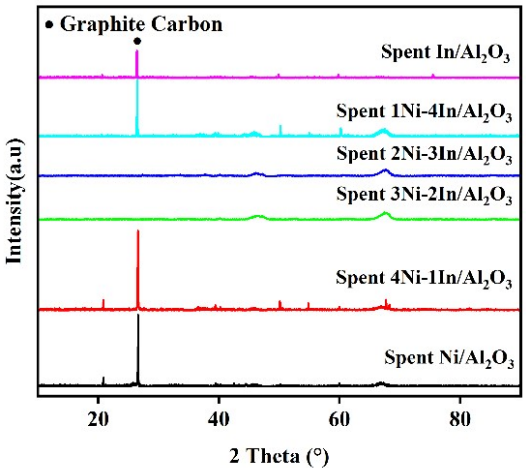

Fig. S6 XRD patterns of the spent catalysts.

The XRD patterns of the spent catalysts are shown in Fig. S6, and compared with the fresh catalysts, it is clearly observed that a strong carbon species peak at 26.6° (JCPDS no. 89-8487) of the Ni/Al_2O_3, In/Al_2O_3, $4Ni\text{-}1In/Al_2O_3$, and $1Ni\text{-}4In/Al_2O_3$, indicating a large amount of carbon generated during the reaction. However, there is no obvious carbon peak for the $2Ni\text{-}3In/Al_2O_3$ catalysts and $3Ni\text{-}2In/Al_2O_3$ catalysts, indicating little or no carbon deposition in these two catalysts during the reaction.

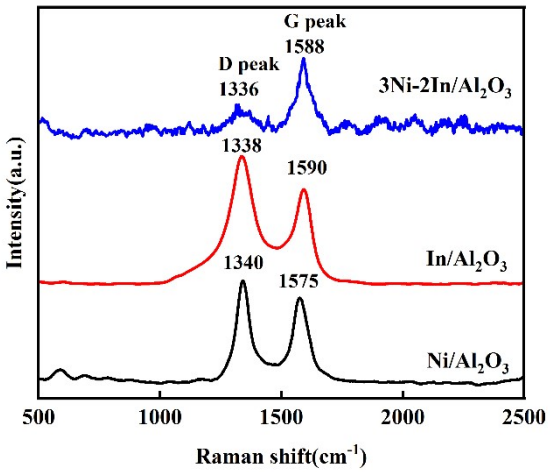

Fig. S7 Raman spectra of the spent catalysts.

In the spectrum, two prominent peaks appear in the wavenumber ranges of 1336-1340 cm^{-1} (D band) and 1575-1590 cm^{-1} (G band). The D band is attributed to structural defects of carbon, representing amorphous carbon or whisker carbon with flaws, while the G-band is attributed to the stretching vibration of the sp^2 bond in ordered graphitic carbon [19]. The intensity of the D-band peaks of the 3Ni-2In/Al_2O_3 catalysts was significantly lower, indicating that the amount of amorphous or whisker carbon produced on the spent 3Ni-2In/Al_2O_3 catalysts was less compared to the other two catalysts The relative intensity between the D and G bands (I_D/I_G) reflects the degree of crystallinity of the carbon deposition. The change in the I_D/I_G ratio of different catalysts is illustrated in Table S4, In/Al_2O_3 catalysts (1.35)> Ni/Al_2O_3 catalysts (1.19)> 3Ni-2In/Al_2O_3 catalyst (0.44). The I_D/I_G ratio for the spent Ni/Al_2O_3 and In/Al_2O_3 catalysts is more than 1, which indicates that the crystallinity of carbon deposition generated on these two monometallic catalysts is low, and the carbon generated is mainly amorphous carbon or filamentary carbon, and it can be known from the results of TG and TEM that the carbon deposition generated on the In/Al_2O_3 catalysts is amorphous carbon and that the carbon generated on the Ni/Al_2O_3 catalysts is mainly filamentary carbon. For the 3Ni-2In/Al_2O_3 catalyst, the heights of the D-band peak and G-band peak were significantly lower than the Ni/Al_2O_3 and In/Al_2O_3, indicating that

less carbon was generated on the catalyst during the reaction process. The I_D/I_G ratio was 0.44, indicating that the carbon generated during the reaction process exhibited higher crystallinity and graphite carbon is formed, and the graphitic carbon generated can be oxidized by CO_2 to form CO without affecting the DRM reaction.

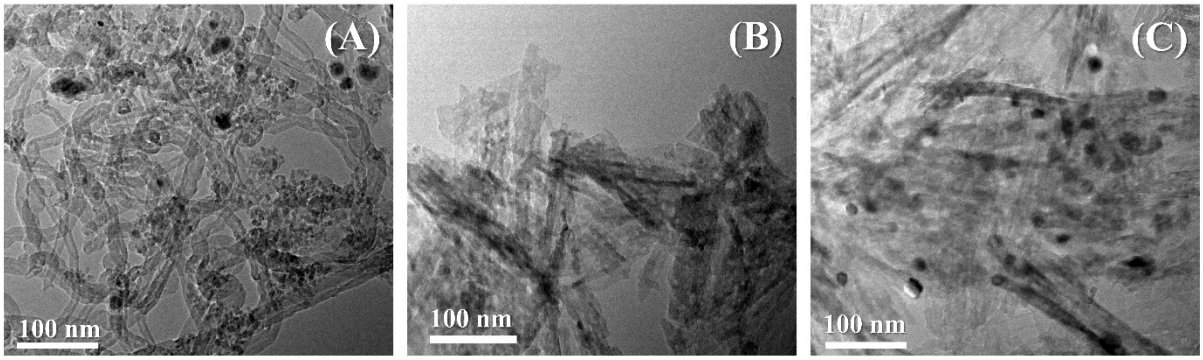

Fig. S8 TEM images of spent Ni/Al_2O_3 (A), In/Al_2O_3 (B), and $3Ni\text{-}2In/Al_2O_3$ (C).

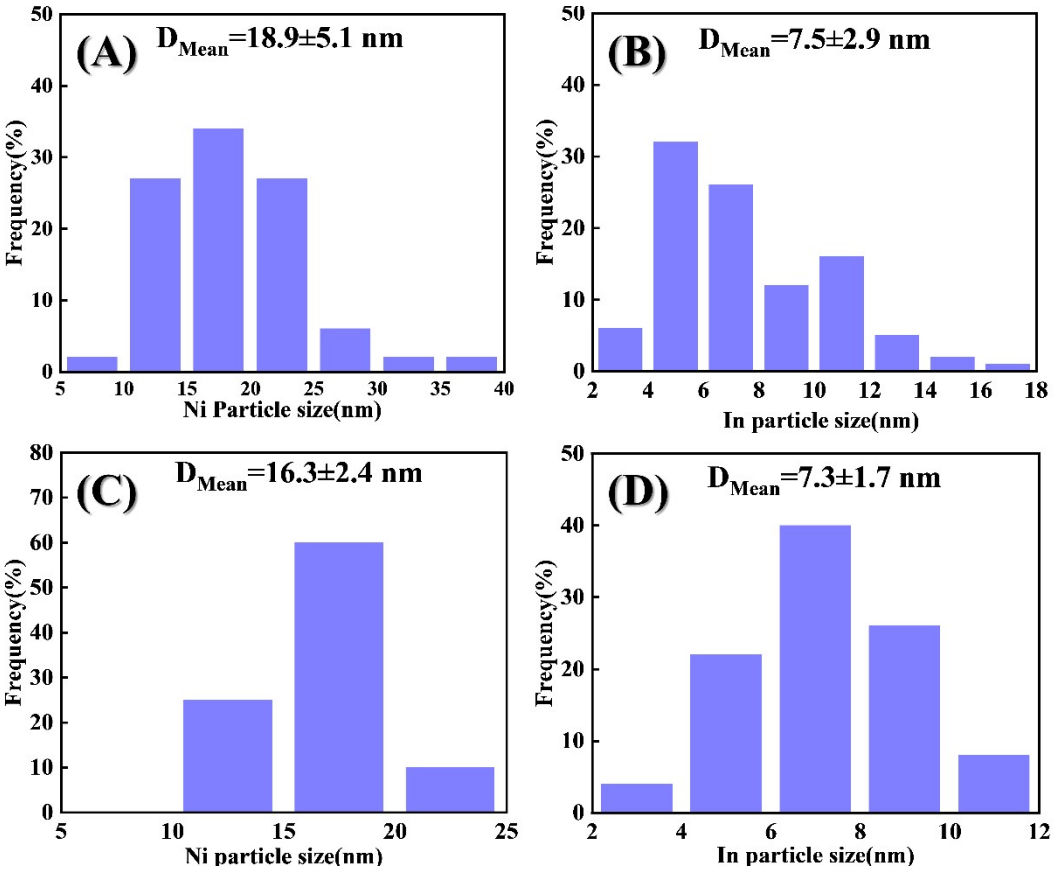

Fig. S9 Particle size distributions of Ni and In in the (A) spent Ni/Al_2O_3, (B) spent In/Al_2O_3, (C) and (D) spent $3Ni\text{-}2In/Al_2O_3$ catalyst.

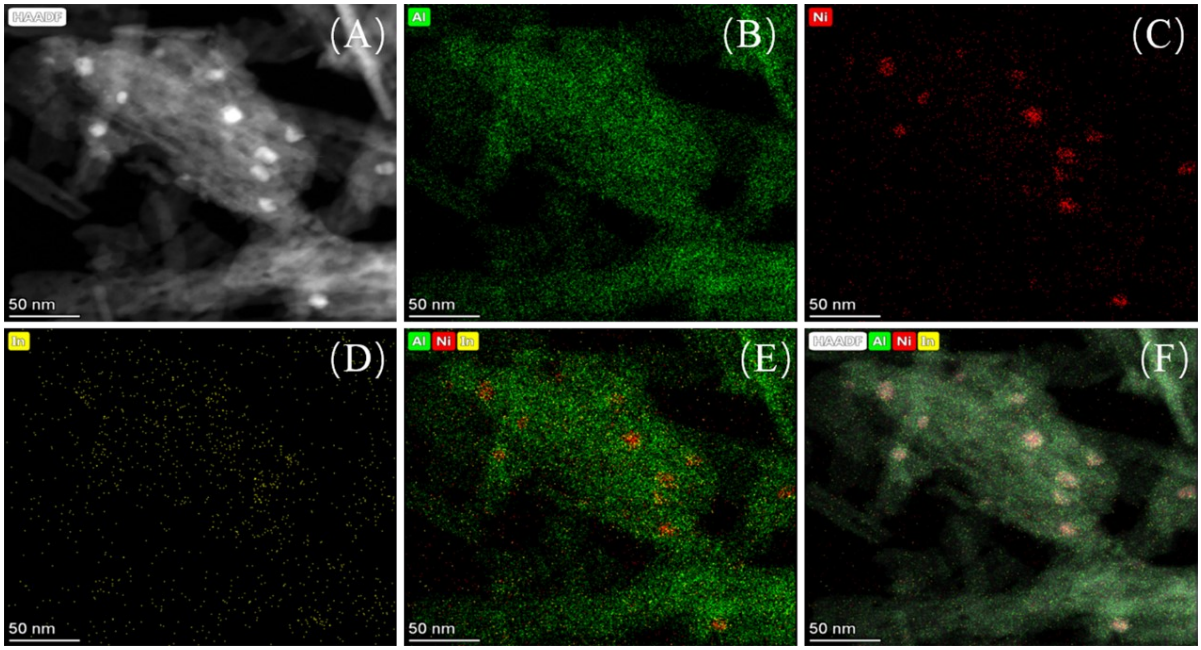

Fig. S10. HAADF-STEM images (A) and EDS profile of Al (B), Ni (C), In (D), and merged images (E) and (F) in spent Ni-In/Al_2O_3 catalyst.

A typical HAADF-STEM image and the corresponding elemental mapping reveal the elemental distributions of Ni, In, and Al in the spent Ni–In/Al_2O_3 samples, as shown in Fig. S10. The Ni particles in the spent catalysts were found to be more uniformly distributed than those in the reduced catalysts. This is due to the interaction between the two metals during the reaction, the instability of the In oxides increases the concentration of reactive oxygen near Ni, suppressing the agglomeration effect of Ni particles and making the reaction more active, and the Ni particles are more dispersed in the spent catalyst than in the reduced catalyst, the uniformly dispersed Ni reduces the emergence of carbon species during the reaction process, enhancing DRM stability.

References

1. W. Liu, L. Li, S. Lin, Y. Luo, Z. Bao, Y. Mao, K. Li, D. Wu and H. Peng, *J. Energy Chem.*, 2022, **65**, 34-47.
2. A. Horváth, M. Németh, A. Beck, B. Maróti, G. Sáfrán, G. Pantaleo, L. F. Liotta, A. M. Venezia and V. La Parola, *App. Catal. A Gen.*, 2021, **621**, 118174.
3. J. Károlyi, M. Németh, C. Evangelisti, G. Sáfrán, Z. Schay, A. Horváth and F. Somodi, *J. Ind. Eng. Chem.*, 2018, **58**, 189-201.
4. H. Arbag, S. Yasyerli, N. Yasyerli, G. Dogu and T. Dogu, *Appl. Catal. B Environ.*, 2016, **198**, 254-265.
5. J. Huang, Y. Yan, S. Saqline, W. Liu and B. Liu, *Appl. Catal. B Environ.*, 2020, **275**, 119109.
6. E. Akiki, D. Akiki, C. Italiano, A. Vita, R. Abbas-Ghaleb, D. Chlala, G. Drago Ferrante, M. Laganà, L. Pino and S. Specchia, *Int. J. Hydrogen Energ.*, 2020, **45**, 21392-21408.
7. D. Li, S. Xu, K. Song, C. Chen, Y. Zhan and L. Jiang, *Appl. Catal., A*, 2018, **552**, 21-29.
8. M. Zhang, J. Zhang, Z. Zhou, S. Chen, T. Zhang, F. Song, Q. Zhang, N. Tsubaki, Y. Tan and Y. Han, *Appl. Catal. B Environ.*, 2020, **264**, 118522.
9. X. Wang, Y. Liu and K. Liu, *Int. J. Hydrogen Energ.*, 2020, **45**, 28325-28336.
10. G. Wang, Y. Liang, J. Song, H. Li and Y. Zhao, *Front Chem*, 2020, **8**, 220.
11. A. Jawad, F. Rezaei and A. A. Rownaghi, *Catal. Today*, 2020, **350**, 80-90.
12. S. Chu, Z. Cai, M. Wang, Y. Zheng, Y. Wang, Z. Zhou and W. Weng, *Nanoscale*, 2020, **12**, 20922-20932.
13. S. A. Shin, Y. S. Noh, G. H. Hong, J. I. Park, H. T. Song, K.-Y. Lee and D. J. Moon, *J. Taiwan. Inst. Chem. E.*, 2018, **90**, 25-32.
14. J.-H. Park, S. Yeo, I. HeO and T.-S. Chang, *App. Catal. A Gen.*, 2018, **562**, 120-131.
15. S. Das, M. Sengupta, A. Bag, M. Shah and A. Bordoloi, *Nanoscale*, 2018, **10**, 6409-6425.
16. A. Al-Fatesh, A. Ibrahim, J. Abu-Dahrieh, A. Al-Awadi, A. El-Toni, A. Fakeeha and A. Abasaeed, *Catalysts*, 2018, **8**, 229.
17. Y. Zhu, S. Zhang, B. Chen, Z. Zhang and C. Shi, *Catal. Today*, 2016, **264**, 163-170.
18. L. Jin, B. Ma, S. Zhao, X. He, Y. Li, H. Hu and Z. Lei, *Int. J. Hydrogen Energy*, 2018, **43**, 2689-2698.
19. J. G. Roblero, F. Pola-Albores, M. A. Valenzuela, E. Rojas-García, E. Ríos-Valdovinos and G. Valverde-Aguilar, *Int. J. Hydrogen Energ.*, 2019, **44**, 10473-10483.